iScience

CellPress
OPEN ACCESS

Article

A cantilever-structure triboelectric nanogenerator for energy harvesting and defect detection via long short-term memory network

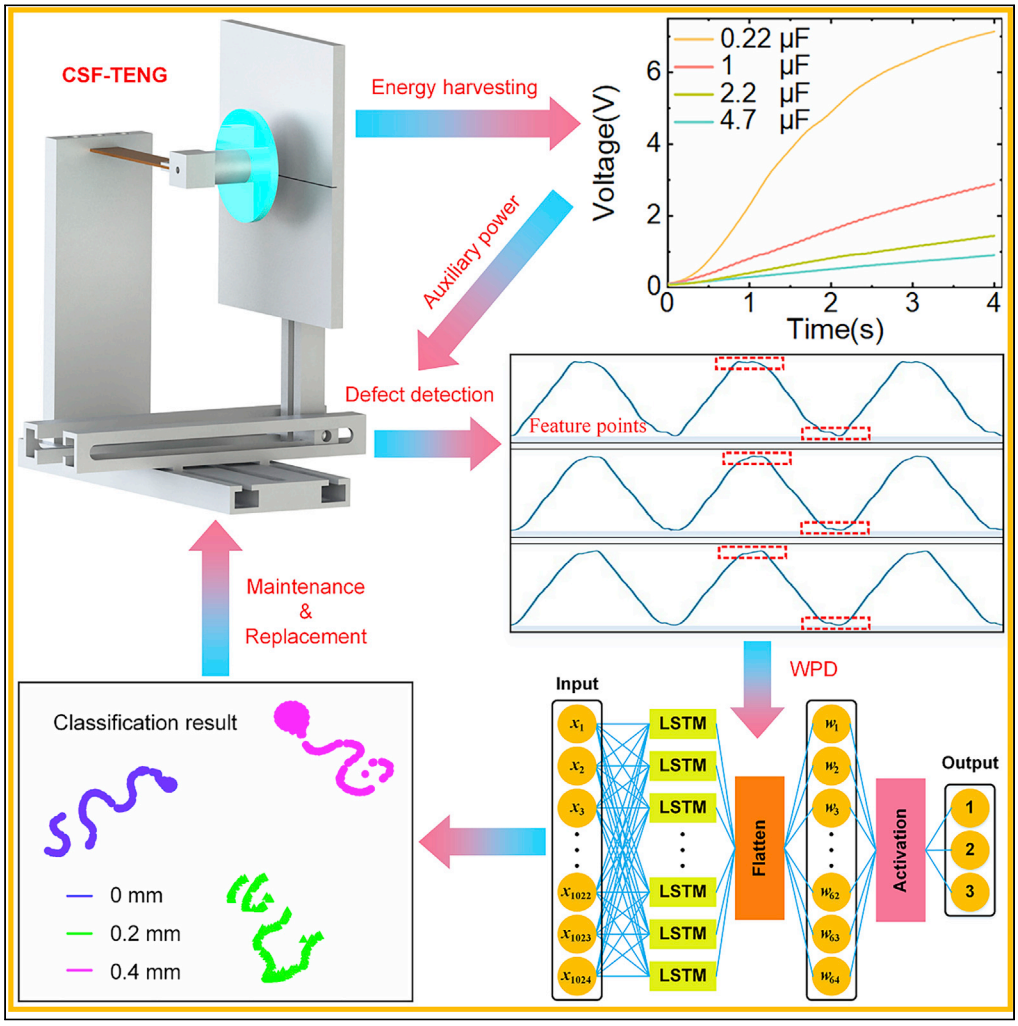

Chuanfu Xin, Zifeng Xu, Ying Gong, Hengyu Guo, Zhongjie Li, Jiheng Ding, Shaorong Xie

lizhongjie@shu.edu.cn (Z.L.)
ding_jiheng@shu.edu.cn (J.D.)
srxie@shu.edu.cn (S.X.)

Highlights

A novel TENG is proposed to harvest energy and detect defects

The 0.22, 1, and 2.2 μF capacitors are charged to 7.1, 2.9, and 1.4 V within 4s

The accuracy of the cantilever defect identification model is 98.6%

Xin et al., iScience 25, 105673
December 22, 2022
https://doi.org/10.1016/j.isci.2022.105673

iScience

CellPress
OPEN ACCESS

Article

A cantilever-structure triboelectric nanogenerator for energy harvesting and defect detection via long short-term memory network

Chuanfu Xin,[1] Zifeng Xu,[1] Ying Gong,[1,3] Hengyu Guo,[4] Zhongjie Li,[1,3,*] Jiheng Ding,[1,*] and Shaorong Xie[2,5,*]

SUMMARY

The electric signals of cantilever energy harvesting devices with/without a crack were mainly obtained by external sensors, so detecting device damage on a large scale is difficult. To tackle the issue, a cantilever-structure freestanding triboelectric nanogenerator (CSF-TENG) device was proposed, which can scavenge ambient energy and act as a self-powered sensor. Firstly, the relation between the peak-to-peak voltage and amplitude of the CSF-TENG was established. Next, the output performance of the CSF-TENG was measured. Then, depending on electric signals output by the CSF-TENG, a cantilever defect identification model was built by using the wavelet packet and long short-term memory (LSTM) algorithms. The experimental results manifest that the accuracy of the model is about 98.6%. Thus, the CSF-TENG with a crack can be detected timely due to its self-monitoring ability, which is of great significance for the development of self-powered sensor networks.

INTRODUCTION

With the rapid development of big data and Internet of Things, billions of low-power sensors powered by chemical batteries are used. Due to the short lifespan, high cost of regular replacement, and environmental pollution of chemical batteries, how to power sensor networks has become an urgent problem. To solve the problem, researchers have proposed some methods to scavenge ambient energy, such as wind,[1–3] water,[4–6] and mechanical vibration.[7–9] Now, the commonly used methods for harvesting ambient energy mainly include electromagnetic,[10–12] piezoelectric,[13–15] triboelectric nanogenerator (TENG),[16–18] electrostatic,[19,20] and magnetostrictive.[21,22] Due to the advantages of simple fabrication, lightweight, high power density, low cost, and diverse materials, TENGs have been widely used for harvesting ambient energy since 2012.

Due to the advantages of high sensitivity and without applying an external power source, TENGs have also attracted considerable attention for acting as self-powered sensors. Yu et al.[23] developed a particles-laden droplet-driven triboelectric nanogenerator to monitor sediment particle parameters. Based on deep learning method, the identifying accuracy achieves 96%. Garcia et al.[24] reported a self-powered impact sensor using triboelectric nanogenerators for estimating small energy impacts. According to the experimental results, the output voltages and currents increase under the higher energy impacts, and the impact sensitivity of 14 V/J and 901 nA/J is achieved. Zhao et al.[25] proposed a clock pointer-like triboelectric nanogenerator to form a self-powered wind speed sensor. Due to the higher accuracy of algorithm parameters, the self-powered sensor displays a superior performance for detecting wind speed. Zhang et al.[26] investigated a self-powered sensor based on triboelectric nanogenerators to monitor the driver's steering actions. The experimental results manifest that the detection accuracy is 92%, demonstrating the potential of triboelectric nanogenerators as action detection sensors. Zhang et al.[27] designed a liquid-solid triboelectric nanogenerator as a self-powered sensor to detect liquid leakage. The experimental results show that the sensor is sensitive to small liquid leakage and the classification accuracy is over 90%. In addition, many sensors based on triboelectric nanogenerators were proposed, such as self-powered acceleration sensors,[28–31] self-powered flowmeters,[32,33] sound monitoring and identification sensors,[34,35] vibration frequency monitoring sensors,[36,37] etc.

Furthermore, based on the advantages of self-powered sensors, many researchers have utilized them to detect engineering structure damage. Han et al.[38] investigated a bearing fault diagnosis technology by

[1]School of Mechatronic Engineering and Automation, Shanghai University, Shanghai 200444, P.R. China

[2]School of Computer Engineering and Science, Shanghai University, Shanghai 200444, P.R. China

[3]Engineering Research Center of Unmanned Intelligent Marine Equipment, Shanghai University, Shanghai 200444, P.R. China

[4]Department of Applied Physics, Chongqing University, Chongqing 400044, P.R. China

[5]Lead contact

*Correspondence: lizhongjie@shu.edu.cn (Z.L.), ding_jiheng@shu.edu.cn (J.D.), srxie@shu.edu.cn (S.X.)

https://doi.org/10.1016/j.isci.2022.105673

using triboelectric nanogenerators as a self-powered sensor. Compared to the results of five algorithms, the classification accuracy of the CNN algorithm is the highest, exceeding 99%. Zhao et al.[39] studied a self-powered vibration accelerometer based on triboelectric nanogenerators to monitor railway states. According to the experimental results, the output voltages and currents of the triboelectric nanogenerator are linearly related to the vibration acceleration, which demonstrates the potential of the accelerometer for fault diagnosis. Park et al.[40] proposed a sponge-typed triboelectric nanogenerator as a motor fault detector. By measuring the vibration of a motor, the faulty motor can be detected indirectly. Besides, Li et al.[41] developed a ball-bearing structured triboelectric nanogenerator to detect defects, Guo et al.[42] reported a triboelectric nanogenerator as a self-powered sensor to identify mechanical faults, and Chen et al.[43] presented a self-powered resonant sensor for recognizing damage.

Because of the advantages of easy fabrication and installation, effective scavenging low-frequency vibration energy, and so on, the devices based on cantilever structure are commonly used to harvest ambient energy.[44–46] However, during the operation of cantilever-structure energy harvesting devices, cracks are usually inevitable in the overstress area of cantilevers. Aiming at defect detection of cantilevers, Zhao et al.[47] used a feedback voltage output of piezoelectric sensors to change the stiffness at local section of the beam and amplify the natural frequency change of the beam caused by cracks, so defects can be easily identified. Deng et al.[48] developed a vision-based cantilever defect identification technology, which can effectively diagnose different sizes and positions of cracks according to the experimental results. Samourgkanidis et al.[49] utilized magnetoelastic vibration sensors to obtain the bending modes of cantilevers and established the relation between bending modes and cracks. Then, the optimum corresponding crack can be found by the pattern-matching method, and the identification error is approximately 11.4%. Suzuki et al.[50] applied the wireless surface acoustic wave sensor to detect the vibration of cantilevers, and took advantage of machine learning methods to evaluate cantilever damage. According to the experimental results, the accuracy of the machine learning method is about 90%. Gupta et al.[51] adopted the Bruel & Kjaer instrument to extract the frequency response of cantilevers, and used an artificial neural network algorithm to identify the damage severity and locations of cantilevers. Zhao et al.[52] presented a method based on laser Doppler to obtain the vibration time-domain signal of cantilevers, and adopted fast Fourier, continuous wavelet transform, and convolutional neural network methods to identify defects. Based on the experimental results, the average accuracy is 90.6%.

According to the above references, most of the electric signals of cantilevers were obtained by using external sensors, which require chemical batteries or other energy storage devices to power them, leading to the difficulty in detecting energy harvesting device defects on a large scale, high replacement costs, environmental pollution problems, etc. In addition, due to piezoelectric materials with the characteristics of brittleness, easy broken under impact loads, and complex installation, it is difficult to apply to curved structures with great change in amplitude. Herein, a cantilever-structure triboelectric nanogenerator was proposed, which has two working modes, i.e., harvesting ambient energy and acting as a self-powered sensor. The main contributions are as follows: (1) designing a cantilever-structure freestanding triboelectric nanogenerator (CSF-TENG); (2) establishing the relation between the peak-to-peak voltage and amplitude of the CSF-TENG, which was demonstrated by open-circuit voltage, and short-circuit current experiments; (3) utilizing the wavelet packet algorithm to preprocess electric signal data and improve the accuracy of the defect identification model; and (4) building a defect identification model based on the long short-term memory algorithm.

RESULTS AND DISCUSSION

Fabrication of TENG

To avoid the influence of the contact force between two triboelectric layers on the vibration behavior of the beam itself, a freestanding triboelectric nanogenerator was designed. All experimental materials, such as polyimide (PI), sponge, polytetrafluoroethylene (PTFE), graphite paper (Gp), and nickel cloth were purchased from a local market (as shown in key resources table) and used without further treatment. The device attached to the positive triboelectric layer is made of aluminum material, so a 0.15 mm thick PI layer was used as a substrate to prevent the output performance of TENGs from being affected. According to previous studies,[2] a soft substrate can increase the contact area between triboelectric layers and improve the output performance of TENGs. Thus, to increase the contact area between triboelectric layers, a 2 mm thick sponge was used as a buffer layer. Then, PTFE, Gp, and nickel cloth act as negative triboelectric layers, positive triboelectric layers, and electrodes, respectively, and their thicknesses are 0.05, 0.05, and 0.1 mm. The

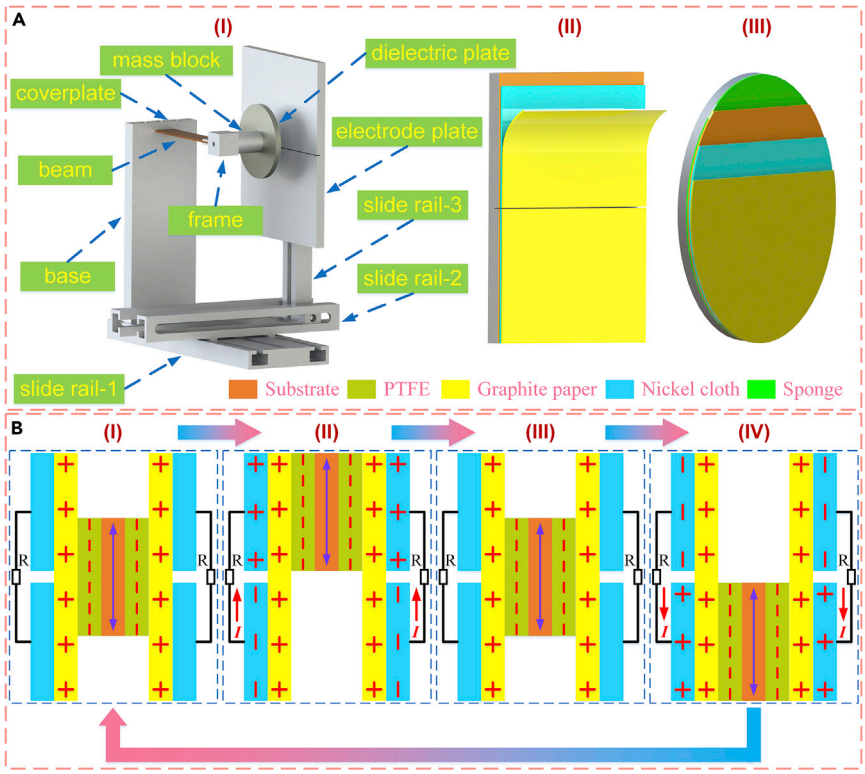

Figure 1. The configuration and working principle of the CSF-TENG

(A) The configuration of the CSF-TENG.

(B) The working principle of the CSF-TENG.

negative triboelectric layer was attached to an acrylic plate with a diameter of 40 mm, which was connected to cantilevers by screws. Compared to the negative triboelectric layer, the size of the positive triboelectric layer is larger, namely, 80 × 100 mm, and this is because the amplitude of the cantilever increases significantly under strong excitation. Besides, to avoid the influence of wires on the contact area of triboelectric layers, the size of electrodes of the negative triboelectric layer was set to 85 × 49.8 mm.

Working principle

In this paper, the device is a symmetrical structure, and the left half of the device is shown in Figure 1A. As shown in Figure 1A(I), the device consists of slide rail-1, slide rail-2, slide rail-3, electrode plate, dielectric plate, mass block, cover-plate, beam, base, and frame, which were connected by screws. Especially, slide rail-1, slide rail-2, and slide rail-3 can be moved, so the relative position and initial distance between the electrode plate and the dielectric plate can be adjusted. As shown in Figure 1A(II), the two electrodes were attached to the electrode plate, which is divided into upper and lower parts, and then the positive triboelectric layer was attached to the two electrodes. The negative triboelectric layer was attached to the dielectric plate with a diameter of 40 mm, as shown in Figure 1A(III). In addition, the mechanical object model of the device is depicted in Figure S1. The overall dimensions of the device and boards are shown in Figure S2, and the specification of the cantilever beam is 64 × 12 × 1 mm.

Figure 1B displays the working principle of the CSF-TENG. When the cantilever is not excited, the initial position of the negative triboelectric layer is illustrated in Figure 1B(I). Due to the different abilities in attracting electrons for PTFE and Gp materials, a large number of negative charges are accumulated on the surface of PTFE, so the surface of Gp remains an equal amount of positive charges. When the cantilever is excited, the negative triboelectric layer moves upward, as shown in Figure 1B(II). According to the effect of triboelectrification and electrostatic induction, the upper and lower electrodes induce positive and negative charges, respectively, and the current flows from the lower electrode to the upper electrode.

Next, when the negative triboelectric layer moves to the maximum position above, the upper and lower electrodes are in an electrostatic equilibrium state, and no current is generated in external circuits. Then, the negative triboelectric layer moves downward until the maximum position below, and the current flows from the upper electrode to the lower electrode, as described in Figure 1B(III) and (IV). Finally, the negative triboelectric layer returns to the original position. Under the triboelectric layers of graphite paper and PTFE, we performed simulations in COMSOL Multiphysics 5.6. First, the sizes of graphite paper, PTFE, and electrodes were set to 100 × 80 mm, a diameter of 40 mm, and 49.8 × 80 mm, and the distance between two electrodes is 0.4 mm. Then, the equally positive and negative charges were added to the graphite paper and PTFE, which remain constant in all simulations. Based on different positions of the PTFE triboelectric layer, the simulation results are depicted in Figure S3.

As shown in Figure S4A, the experimental platform consists of the PC, controller (Econ VT-9002), power amplifier (Econ E5874A), accelerometer (Econ EA-YD-181), and shaker (Econ E-JZK- 50). The device was fixedly connected to the shaker, and the accelerometer was fixed on slide rail-1 with tape. Firstly, the controller receives the instructions from the PC and generates control signals, which are transmitted to the power amplifier to drive the shaker. Then, the accelerometer transmits feedback signals to the controller, so the CSF-TENG can operate under constant excitation. The open-circuit voltages and short-circuit currents of the CSF-TENG were measured by an oscilloscope (Tektronix MDO3024) and an electrometer (Keithley 6514), respectively, and the testing circuits are displayed in Figure S4B.

The output performance of the CSF-TENG

According to the working principle of freestanding TENGs, the relation between the peak-to-peak voltage and amplitude of the CSF-TENG was established. As shown in Figure S5, we assume that dk is a small region in the bottom dielectric surface, which contains tribo-charges with a density of σ. Therefore, the total charges on metal 1 and metal 2 can be described as σwdk. In addition, the thickness of the positive triboelectric layer and electrode gap are h and g, respectively. Thus, the total charges of metal 1 and metal 2 (dQ_1 and dQ_2) can be calculated by using the following equations under the short-circuit conditions,

$$dQ_1 = \frac{\sigma w dk}{1+\frac{C_2(k)}{C_1(k)}} \quad \text{(Equation 1)}$$

$$dQ_2 = \frac{\sigma w dk}{1+\frac{C_1(k)}{C_2(k)}} \quad \text{(Equation 2)}$$

where, $C_i(k)$ is the capacitance between this small region dk and metal i (i is 1, and 2.), and w is the width of triboelectric layers.

According to the principle of superposition of electrostatic fields, the total charges on metal 1 and metal 2 can be shown as:

$$Q_1 = \sigma w \int_0^l \frac{dk}{1+\frac{C_2(k)}{C_1(k)}} \quad \text{(Equation 3)}$$

$$Q_2 = \sigma w \int_0^l \frac{dk}{1+\frac{C_1(k)}{C_2(k)}} \quad \text{(Equation 4)}$$

where, l is the length of the dielectric layer.

Therefore, the short-circuit charges (ΔQ) between metal 1 and metal 2 can be shown as:

$$\Delta Q = \sigma w \left(\int_0^l \frac{dk}{1+\left(\frac{C_2(k)}{C_1(k)}\right)_{L=x}} - \int_0^l \frac{dk}{1+\left(\frac{C_1(k)}{C_2(k)}\right)_{L=0}} \right) \quad \text{(Equation 5)}$$

When the cantilever is excited, the dielectric plate swings in the vertical direction, so the ambient energy is converted into electrical energy. According to the working principle of freestanding TENGs, the relation

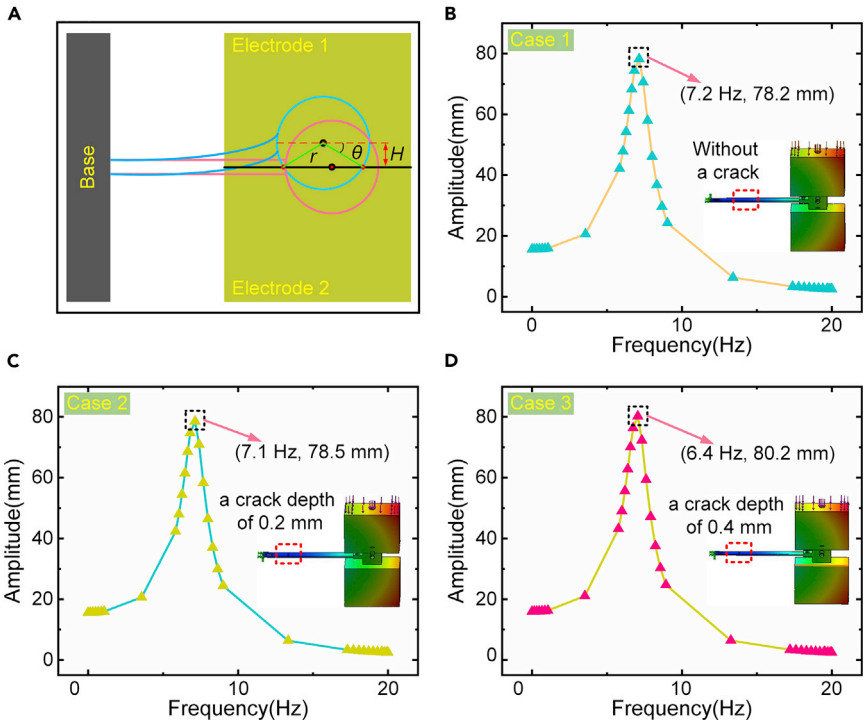

Figure 2. The motion relation and simulation results of the cantilever

(A) The motion relation of the cantilever.

(B–D) the simulation results under the cantilever (B) without a crack, (C) with a crack depth of 0.2 mm, and (D) with a crack depth of 0.4 mm.

between peak-to-peak voltage (V) and the amplitude (H) of the dielectric plate can be explained with the following formula:

$$V = \frac{\Delta Q}{C} = \frac{\sigma \Delta S}{C} \quad \text{(Equation 6)}$$

where, C is the equivalent capacitance between the two electrodes, and ΔS is calculated by the following formula:

$$\Delta S = \frac{\pi \theta r^2}{180^{\circ}} + Hr\cos(\theta) \quad \text{(Equation 7)}$$

In addition, θ can be obtained with the following equation:

$$\sin(\theta) = \frac{H}{r} \quad \text{(Equation 8)}$$

As shown in Figure 2A, r and H are the radius and amplitude of the dielectric plate.

The final expressions of the peak-to-peak voltage (V) and amplitude (H) are expressed in Equation 9.

$$V = \frac{\sigma}{C}\left(\frac{\pi r^2 \arcsin(H/r)}{180} + Hr\cos(\arcsin(H/r))\right) \quad \text{(Equation 9)}$$

According to the equations above, the output voltages of the CSF-TENG increase as the amplitude of the dielectric plate rises. To compare the output performance change of the CSF-TENG with/without a crack, we first performed simulations by using SolidWorks 2018. The simulation conditions were set as follows: the excitation frequency range was set to 0–20 Hz, the force applied on the end mass surface is 15 N (uniformly distributed), and the modal damping was set to 0.1. As shown in Figure 2B, when the cantilever has no a crack, under the harmonic excitation, the amplitude of the cantilever first increases and then decreases with the increment of the excitation frequency. When the excitation frequency is 7.2 Hz, the amplitude of the cantilever reaches a maximum, i.e., 78.2 mm. When the crack depth of the cantilever is 0.2 mm,

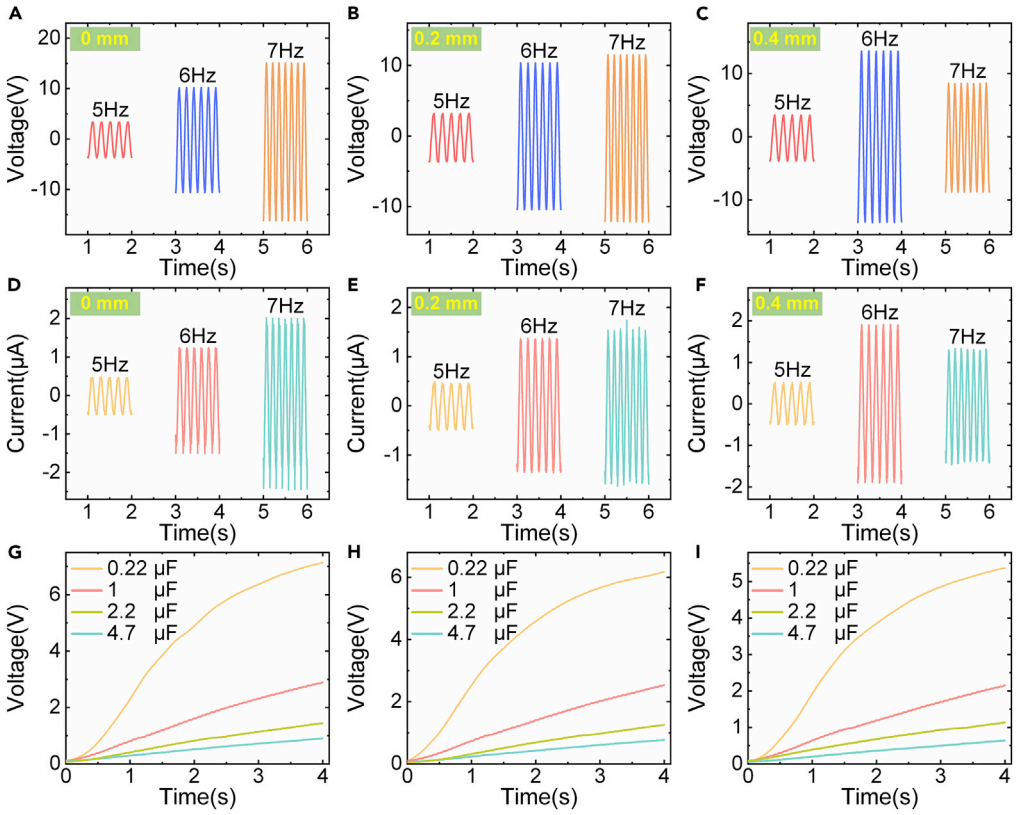

Figure 3. The output performance of the CSF-TENG with/without a crack

(A–C) the output voltages of the CSF-TENG (A) without a crack, (B) with a crack depth of 0.2 mm, and (C) with a crack depth of 0.4 mm.

(D–F) the output currents of the CSF-TENG (D) without a crack, (E) with a crack depth of 0.2 mm, and (F) with a crack depth of 0.4 mm.

(G–I) the charging performance of the CSF-TENG (G) without a crack, (H) with a crack depth of 0.2 mm, and (I) with a crack depth of 0.4 mm.

the amplitude change of the cantilever is similar to that of the cantilever without a crack. When the excitation frequency is 7.1 Hz, the amplitude of the cantilever with a crack depth of 0.2 mm is 78.5 mm, as depicted in Figure 2C. Furthermore, the simulation of the cantilever with a crack depth of 0.4 mm was performed, as illustrated in Figure 2D. When the excitation frequency is 6.4 Hz, the amplitude of the cantilever with a crack depth of 0.4 mm is 80.2 mm. Compared to case 1, case 2, and case 3, the amplitude of the cantilever with a crack depth of 0.4 mm is the largest. In addition, the amplitude of the CSF-TENG gradually increases as the excitation frequency rises and approaches the resonant frequency, so different amplitudes can be obtained at diverse excitation frequencies (such as 5, 6, and 7 Hz). According to the above simulation results, as the crack depth increases, the natural frequency of cantilevers decreases, and the amplitude rises under the resonant frequency, which is because the stiffness of cantilevers declines. In addition, the object pictures of cantilevers with/without a crack are displayed in Figure S6.

Then, we carried out experiments of open-circuit voltages, short-circuit currents, and charging capacitors, as shown in Figure 3. The experimental conditions were set as follows: the excitation acceleration is 0.4 g, and the excitation frequencies are 5, 6, and 7 Hz.

Firstly, the open-circuit voltages of the CSF-TENG with/without a crack were measured. As shown in Figure 3A, when the CSF-TENG is defect-free, the peak-to-peak voltage of the CSF-TENG is 7.2 V under the excitation frequency of 5 Hz. As the excitation frequency increases, the peak-to-peak voltage of the CSF-TENG rises, which verifies Equation 9. When the excitation frequency is 6 and 7 Hz, the peak-to-peak voltage of the CSF-TENG is 20.9 and 31.3 V, respectively. When the CSF-TENG has a crack depth

of 0.2 mm, the peak-to-peak voltage change of the CSF-TENG is similar to that of the CSF-TENG without a crack. Under the excitation frequencies of 5, 6, and 7 Hz, the output voltages of the CSF-TENG with a crack depth of 0.2 mm are 6.9, 20.8, and 23.7 V, respectively, as illustrated in Figure 3B. Furthermore, the peak-to-peak voltage of the CSF-TENG with a crack depth of 0.4 mm was measured. As depicted in Figure 3C, the output voltages of the CSF-TENG with a crack depth of 0.4 mm are 7.3, 27.2, and 17.3 V under the excitation frequencies of 5, 6, and 7 Hz, respectively. According to the experimental results above, the frequency that the output performance of the CSF-TENG with crack depths of 0, 0.2, and 0.4 mm achieves the best decreases gradually, which are consistent with the simulation results that the natural frequency of cantilevers decreases as the crack depth increases.

Next, the short-circuit currents of the CSF-TENG with/without a crack were measured, as shown in Figures 3D–3F. According to the experimental results, the output current change of the CSF-TENG with/without a crack is similar to the output voltage. When the cantilever is defect-free, the output currents of the CSF-TENG are 1, 2.7, and 4.5 μA under the excitation frequencies of 5, 6, and 7 Hz. Similarly, when the cantilever has a crack depth of 0.2 mm, the output currents of the CSF-TENG are 1, 2.7, and 3.4 μA under the excitation frequencies of 5, 6, and 7 Hz. Furthermore, when the cantilever has a crack depth of 0.4 mm, the output currents of the CSF-TENG are 1, 3.8, and 2.8 μA under the excitation frequencies of 5, 6, and 7 Hz. Finally, we utilized the CSF-TENG to perform charging capacitor experiments, and selected capacitors of 0.22, 1, 2.2, and 4.7 μF. Under the excitation frequency of 7 Hz, we implemented charging capacitor experiments by using the CSF-TENG without a crack, as shown in Figure 3G. Within 4 s, the 0.22 μF capacitor was charged to 7.1 V. As the capacitance increases, the voltage of a capacitor decreases. At the same time, the 1, 2.2, and 4.7 μF capacitors were charged to 2.9, 1.4, and 0.9 V, respectively. Similarly, the charging experiments using the CSF-TENG with a crack depth of 0.2 mm were carried out, and the experimental results are displayed in Figure 3H. Within 4 s, the 0.22, 1, 2.2, and 4.7 μF capacitors were charged to 6.2, 2.5, 1.3, and 0.8 V, respectively. Besides, the charging experiments using the CSF-TENG with a crack depth of 0.4 mm were completed, as depicted in Figure 3I. Within 4 s, the 0.22, 1, 2.2, and 4.7 μF capacitors were charged to 5.4, 2.2, 1.2, and 0.7 V, respectively. According to the experimental results above, the aspect that the natural frequency of cantilevers decreases as the crack depth increases was demonstrated again. In addition, we presented a durability test to display the CSF-TENG output over different repetition cycles, as shown in Figure S7.

According to the experimental results of open-circuit voltage, short-circuit current, and charging capacitor, the CSF-TENG can effectively capture ambient energy at low frequencies. Consequently, the CSF-TENG can be used as an auxiliary power to supply electric energy for low-power electronic devices, reducing the number of replacements of power supply units, such as batteries. Therefore, the development of self-powered intelligent sensor networks is possible. To ensure the continuous operation of the CSF-TENG, defect detection of the device is essential. The electrical signal of the CSF-TENG was collected and transmitted to the PC through a management circuit, and then was processed by the defect identification methods to obtain the health state of the device. Based on two aspects, (i) the management circuit is composed of low-power electronic components, and (ii) the state signal of the CSF-TENG was transmitted within a period to reduce power consumption, the CSF-TENG can realize self-monitoring.

The application of the CSF-TENG in defect detection

Through the defect identification technologies, the working state of the CSF-TENG device can be found timely to ensure that they can operate continuously, which is of great significance for the large-scale deployment of self-powered sensor networks. According to the above simulation results, when the cantilever has a crack, the natural frequency and amplitude change slightly. Therefore, the output voltages or currents of the CSF-TENG vary imperceptibly, so it is difficult to identify the cantilever with a crack. However, the voltage waveform of the CSF-TENG with different crack depths changes visibly, as shown in Figure S8. Here, a better strategy that identifies cracks based on the voltage waveform of the CSF-TENG and intelligent algorithms was proposed, such as deep learning models,[53] adaptive wavelet mutation methods,[54] and transfer learning methods.[55]

Figure 4A shows the flow chart of cantilever defect identification based on intelligent algorithms. When the CSF-TENG was excited by the ambient vibration, electric signals were generated, which were collected by an oscilloscope or electrometer as the initial signal data. Then, the health state of the CSF-TENG

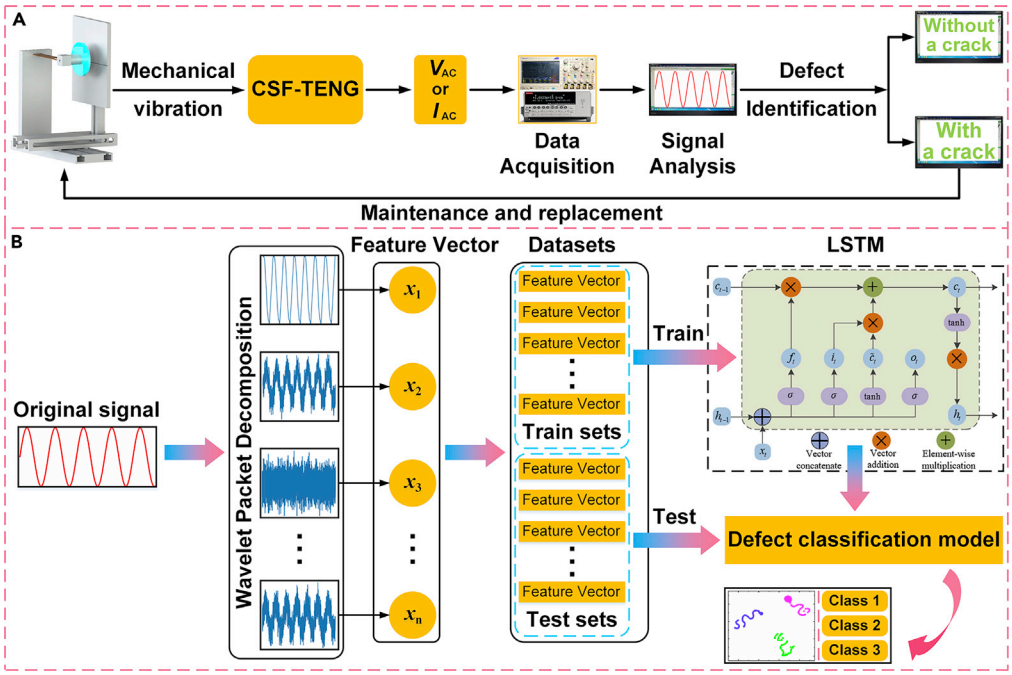

Figure 4. The application of the CSF-TENG in defect detection

(A) Operation flow diagram of the defect detection system based on the CSF-TENG.

(B) The flow diagram of building a defect identification model based on the long short-term memory and wavelet packet algorithms.

device was identified based on the signal analysis model. Due to the advantages of small samples, strong anti-noise ability, and simple network structure, the long short-term memory network has been widely used in the field of defect detection.[56–58] To improve the accuracy of the cantilever defect identification model, the electric signals of the CSF-TENG were first decomposed by using the wavelet packet algorithm. As depicted in Figure 4B, the decomposed signals were used as training sets and test sets to establish a defect classification model based on the long short-term memory algorithm.

In this paper, an oscilloscope was used to acquire electrical signals of the CSF-TENG as sample datasets. To ensure that the characteristic point data of the cantilever with a crack can be collected, the oscilloscope was set as follows: the sampling time is 40 s, and the sampling rate is 25 kS/s, so the dimension of a single sample data is 25,000. Due to the large data dimension, the computational complexity for constructing the defect identification model of the CSF-TENG based on original datasets is enormous. Thus, data preprocessing is very necessary.

In previous studies, many researchers applied the wavelet packet algorithm to the defect identification of mechanical systems and achieved good results.[59,60] Hence, to improve the accuracy of the defect classification model, and reduce the dimension of sample data, the wavelet packet algorithm was used to extract cantilever defect features. Based on high-pass and low-pass filters, the original signal was filtered by the wavelet packet algorithm, and then was converted into 2^j (j is the number of decomposition layers) frequency bands through a two-scale equation, which is as follows:

$$\begin{cases} \psi_{j,n}^{2i}(t) = \sum_k h_k \psi_{j-1,2n-k}^{j}(t) \\ \psi_{j,n}^{2i+1}(t) = \sum_k g_k \psi_{j-1,2n-k}^{j}(t) \end{cases} \quad \text{(Equation 10)}$$

where, $\Psi(t)$ is the mother wavelet, j is the number of decomposition layers, h_k and g_k are a pair of complementary orthogonal mirror filters, n is the middle node number, i is the node number, and k is the frequency band. Then, the wavelet packet coefficient can be calculated by Equation 10.

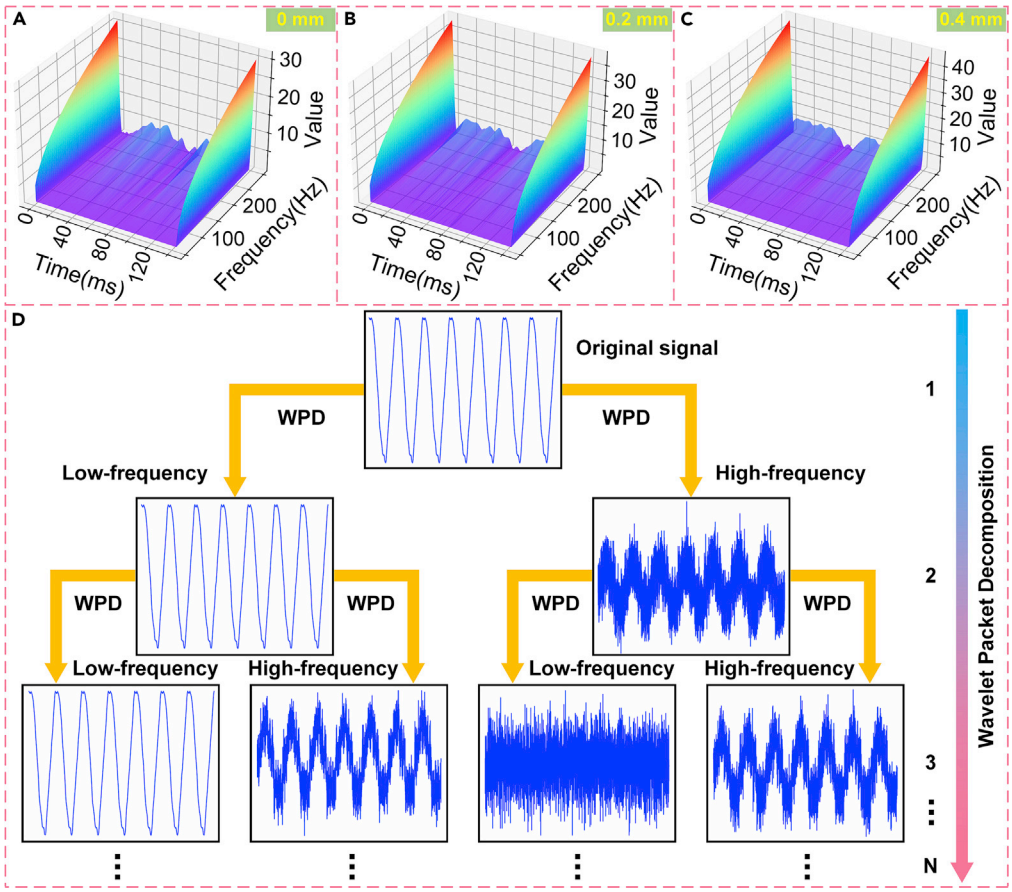

Figure 5. The energy entropy calculation and decomposition of electric signals

(A–C) the energy entropy of electric signals under the CSF-TENG (A) without a crack, (B) with a crack depth of 0.2 mm, and (C) with a crack depth of 0.4 mm.

(D) The decomposition of electric signals.

$$\begin{cases} d_j^{2i}(n) = \sum_k h_k d_{j-1}^i (2n - k) \\ d_j^{2i+1}(n) = \sum_k g_k d_{j-1}^i (2n - k) \end{cases} \quad \text{(Equation 11)}$$

The decomposed signal only changes in form, while the total energy entropy of the signal remains unchanged, which is a measure of the unknown degree of the signal, and represents the number of possible states in the signal and the occurrence probability of these states.[61] The wavelet packet energy entropy is to use the wavelet packet normalized energy feature as the probability distribution of vibration signals to extract the vibration signal features. Therefore, the wavelet packet algorithm can not only effectively reduce the number of feature vectors but also make the defect identification model faster calculation and higher accuracy. Firstly, we calculated the energy entropy of cantilevers by using the wavelet packet algorithm under different crack depths. Figure 5A shows the energy entropy of the cantilever without a crack, which is approximately 28. As the crack depth increases, the energy entropy rises. As shown in Figures 5B and 5C, when the crack depths are 0.2 and 0.4 mm, the energy entropy is about 31 and 41, respectively. According to the experimental results, the energy entropy of cantilevers with different crack depths is diverse, which demonstrates the feasibility of extracting defect features of cantilevers based on wavelet packet decomposition.

Then, the electric signals of cantilevers were decomposed into two parts, i.e., high-frequency and low-frequency information, by using the wavelet packet algorithm. When the decomposition result is not ideal, the wavelet packet algorithm will decompose the high-frequency and low-frequency information again until it

meets the requirements, as shown in Figure 5D. Finally, the decomposed signals were arranged into feature vectors to form training sets and test sets, so a defect classification model can be established based on the long short-term memory (LSTM) algorithm.

The LSTM network is developed based on the recurrent neural network (RNN). When the model parameters remain unchanged, the LSTM, which is suitable for dealing with long complex sequences, can avoid the problem of "gradient disappearance" existing in the RNN network. Compared with traditional recurrent networks, the unit structure of LSTM adds three gated structures: input gate, forget gate, and output gate, so that the model can not only respond to changes in short-term information but also consider the influence of long-term information.

(i) Input gate

The input gate is used to control the current time input information x_t to be saved in the current time long-term memory C_t. The formula is as follows:

$$i_t = \delta(W_i \cdot [h_{t-1}, x_t] + b_i) \quad \text{(Equation 12)}$$

where, δ is the sigmoid function, i_t is the value that allows the current input information C_t to pass, W_i is the coefficient matrix of the fully connected layer of the current input gate, h_{t-1} is the previous time output data, x_t is the current time input data, and b_i is the bias coefficient of the fully connected layer of the current input gate.

(ii) Forget gate

The forget gate is used to control the previous time long-term memory C_{t-1} to be saved in the current time memory C_t. The formula is as follows:

$$f_t = \delta(W_f \cdot [h_{t-1}, x_t] + b_f) \quad \text{(Equation 13)}$$

where, δ is the sigmoid function, f_t is the value that allows the previous time long-term memory C_{t-1} to pass, W_f is the coefficient matrix of the fully connected layer of the current forget gate, h_{t-1} is the previous time output data, x_t is the current time input data, and b_f is the bias coefficient of the fully connected layer of the current forget gate.

(iii) Output gate

The output gate is used to control the output information of the current time memory C_t.

$$o_t = \delta(W_o \cdot [h_{t-1}, x_t] + b_o) \quad \text{(Equation 14)}$$

where, o_t is the value that allows the current time memory C_t output, W_o is the coefficient matrix of the fully connected layer of the current output gate, h_{t-1} is the previous time output data, x_t is the current time input data, and b_o is the bias coefficient of the fully connected layer of the current output gate.

As shown in Figure 6A, the LSTM network contains an LSTM unit layer, a flatten layer, a fully connected layer, and an activation layer. The 1024 × 1 feature vector was successively transferred to the 32 LSTM units and the fully connected layer with 64 neurons, and finally, the classification result was obtained by using the sigmoid function activation. Through open-circuit voltage experiments, we obtained 912 sets of electric signals under cantilevers with crack depths of 0, 0.2, and 0.4 mm, which were divided into training sets and test sets according to the ratio of 7:3. The batch size, epoch, and learning rate were set to 8, 250, and 0.01, respectively. As shown in Figure 6B, when the epoch is small, the training accuracy is low. When the epoch reaches 150, the classification accuracy of the model begins to stabilize. Due to the highly sensitive of TENGs as a self-powered sensor and the effectiveness of the wavelet packet algorithm and long short-term memory network, the accuracy of the model achieved 98.6%. As shown in Figure 6C, the loss value of the model decreases sharply in the initial stage. As the epoch increases, the loss trend of the model is convergence, and finally the loss value of the model is stable at 0.02. To display the performance of the classification model more intuitively, the confusion matrices and classification results of the model are shown in Figures 6D and S9, respectively.

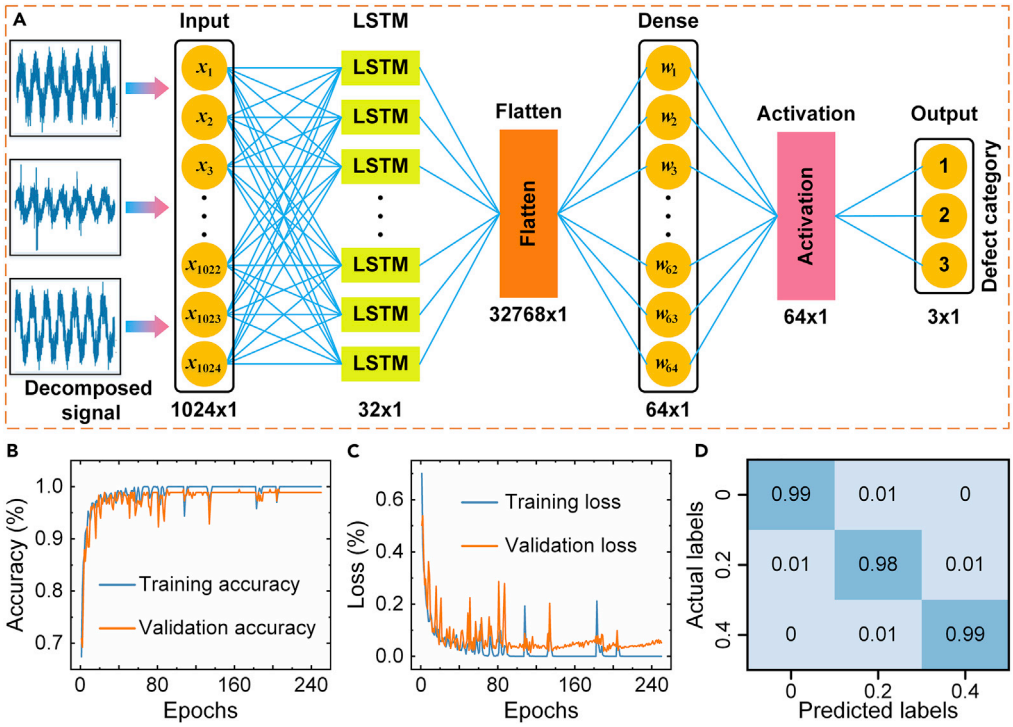

Figure 6. The LSTM network model and defect identification results

(A) The LSTM network model.

(B–D) the (B) accuracy curve, (C) loss curve, and (D) confusion matrices of the defect identification model.

It is worth mentioning that when the wavelet packet algorithm was utilized to decompose the electric signals of cantilevers with/without a crack, the decomposition layers are different, and the performance of the classification model is diverse. When the decomposition layers are 6, 7, 8, and 9, the performance of the model is shown in Figures S10–S13. Compared to the performance of the model with different decomposition layers, when the decomposition layer is 10, the performance of the model is the best. When the decomposition layer increases, the dimension of the feature vector becomes too large, which makes it difficult to establish a classification model. Therefore, the performance of a classification model with more decomposition layers is not further explored.

Conclusions

In this paper, a cantilever-structure energy harvesting device based on triboelectric nanogenerators was proposed, which can scavenge ambient energy and act as a self-powered sensor to detect defects. The main conclusions are as follows:

(1) According to the relative motion of cantilevers, the relation between the peak-to-peak voltage and amplitude of the CSF-TENG was established, which was demonstrated by TENG's output performance experiments under the different amplitudes that were obtained at diverse excitation frequencies.

(2) Under the same harmonic excitation, as the crack depth of the CSF-TENG increases, the natural frequency decreases according to simulation results, which are consistent with experimental results.

(3) Based on the wavelet packet algorithm, the energy entropy of the CSF-TENG with different crack depths is obtained. The experimental results manifest that the energy entropy of the CSF-TENG with crack depths of 0, 0.2, and 0.4 mm are 28, 31, and 41, respectively, which demonstrates the feasibility of the wavelet packet algorithm to extract cantilever defect features.

(4) A cantilever defect identification model was established based on the long short-term memory algorithm. According to the experimental results, when the epoch is 20, the accuracy of the model has

reached about 95%, which shows that the model has a strong learning ability. Eventually, the accuracy of the model stabilized at 98.6%.

In addition, to harvest more energy in one vibration cycle, developing devices with multiple TENG units is necessary. In future work, based on the above work and standard Figure of Merits, an integrated and high-performance TENG device with self-monitoring ability will be designed, which is of great significance for the development of self-powered sensor networks.

Limitations of the study

Although the crack defect detection of cantilevers is realized based on the wavelet packet and long short-term memory network, reaching an accuracy of 98.6%, the dataset for verifying the accuracy of the model is offline data, which was collected by an oscilloscope, so it cannot be applied in practice. In future work, the development of low-power TENG signal acquisition and transmission circuits is necessary to achieve online condition monitoring of energy harvesters.

STAR★METHODS

Detailed methods are provided in the online version of this paper and include the following:

- KEY RESOURCES TABLE
- RESOURCE AVAILABILITY
  - Lead contact
  - Materials availability
  - Data and code availability
- EXPERIMENTAL MODEL AND SUBJECT DETAILS
- METHOD DETAILS
  - Fabrication of CSF-TENG
  - Electrical output signal measurement
- QUANTIFICATION AND STATISTICAL ANALYSIS
- ADDITIONAL RESOURCES

SUPPLEMENTAL INFORMATION

Supplemental information can be found online at https://doi.org/10.1016/j.isci.2022.105673.

ACKNOWLEDGMENTS

This work was supported by National Science Fund for Distinguished Young Scholars (No.: 61625304), Shanghai Sailing Program (No.: 20YF1412700), "Shuguang" Program of Shanghai Education Commission (No.: 20SG40), and Shanghai Outstanding Academic Leaders Plan (No.: 20XD1421700).

AUTHOR CONTRIBUTIONS

C.X. wrote Writing-Original Draft, Z.X. analyzed the data, Y.G., H.G., Z.L., and J.D. revised the manuscript, and S.X. provided funding.

DECLARATION OF INTERESTS

The authors declare no competing interests.

Received: August 22, 2022
Revised: October 21, 2022
Accepted: November 22, 2022
Published: December 22, 2022

REFERENCES

1. He, L., Zhang, C., Zhang, B., Yang, O., Yuan, W., Zhou, L., Zhao, Z., Wu, Z., Wang, J., and Wang, Z.L. (2022). A dual-mode triboelectric nanogenerator for wind energy harvesting and self-powered wind speed monitoring. ACS Nano *16*, 6244–6254. https://doi.org/10.1021/acsnano.1c11658.

2. Xin, C., Guo, H., Shen, F., Peng, Y., Xie, S., Li, Z., and Zhang, Q. (2022). A hybrid generator with electromagnetic transduction for improving the power density of triboelectric nanogenerators and scavenging wind energy. Adv. Mater. Technol. *7*, 2101610. https://doi.org/10.1002/admt.202101610.

3. Fang, Y., Tang, T., Li, Y., Hou, C., Wen, F., Yang, Z., Chen, T., Sun, L., Liu, H., and Lee, C. (2021). A high-performance triboelectric-electromagnetic hybrid wind energy harvester based on rotational tapered rollers aiming at outdoor IoT applications. iScience *24*, 102300. https://doi.org/10.1016/j.isci.2021.102300.

4. Gao, Q., Xu, Y., Yu, X., Jing, Z., Cheng, T., and Wang, Z.L. (2022). Gyroscope-structured triboelectric nanogenerator for harvesting multidirectional ocean wave energy. ACS Nano *16*, 6781–6788. https://doi.org/10.1021/acsnano.2c01594.

5. Yang, Y., Wen, J., Chen, F., Hao, Y., Gao, X., Jiang, T., Chen, B., and Wang, Z.L. (2022). Barycenter self-adapting triboelectric nanogenerator for sea water wave high-entropy energy harvesting and self-powered forecasting in marine meteorology. Adv. Funct. Mater. *32*, 2200521. https://doi.org/10.1002/adfm.202200521.

6. Liu, W., Xu, L., Liu, G., Yang, H., Bu, T., Fu, X., Xu, S., Fang, C., and Zhang, C. (2020). Network topology optimization of triboelectric nanogenerators for effectively harvesting ocean wave energy. iScience *23*, 101848. https://doi.org/10.1016/j.isci.2020.101848.

7. Xu, Z., Li, D., Wang, K., Liu, Y., Wang, J., Qiu, Z., Wu, C., Lin, J., Guo, T., and Li, F. (2022). Stomatopod-inspired integrate-and-fire triboelectric nanogenerator for harvesting mechanical energy with ultralow vibration speed. Appl. Energy *312*, 118739. https://doi.org/10.1016/j.apenergy.2022.118739.

8. Liu, N., Liu, D., Gao, Y., Li, S., Zhou, L., Zhao, Z., Cui, S., Liu, L., Wang, Z.L., and Wang, J. (2022). A tuning-fork triboelectric nanogenerator with frequency multiplication for efficient mechanical energy harvesting. Small Methods *6*, 2200066. https://doi.org/10.1002/smtd.202200066.

9. Zhao, X., Li, C., Wang, Y., Han, W., and Yang, Y. (2021). Hybridized nanogenerators for effectively scavenging mechanical and solar energies. iScience *24*, 102415. https://doi.org/10.1016/j.isci.2021.102415.

10. Li, Z., Jiang, X., Yin, P., Tang, L., Wu, H., Peng, Y., Luo, J., Xie, S., Pu, H., and Wang, D. (2021). Towards self-powered technique in underwater robots via a high-efficiency electromagnetic transducer with circularly abrupt magnetic flux density change. Appl. Energy *302*, 117569. https://doi.org/10.1016/j.apenergy.2021.117569.

11. Peng, Y., Zhang, L., Li, Z., Zhong, S., Liu, Y., Xie, S., and Luo, J. (2022). Influences of wire diameters on output power in electromagnetic energy harvester. Int. J. Precis. Eng. Manuf. Green Tech. 1–12. https://doi.org/10.1007/s40684-022-00446-8.

12. Li, Z., Xin, C., Peng, Y., Wang, M., Luo, J., Xie, S., and Pu, H. (2021). Power density improvement of piezoelectric energy harvesters via a novel hybridization scheme with electromagnetic transduction. Micromachines *12*, 803. https://doi.org/10.3390/mi12070803.

13. Peng, Y., Xu, Z., Wang, M., Li, Z., Peng, J., Luo, J., Xie, S., Pu, H., and Yang, Z. (2021). Investigation of frequency-up conversion effect on the performance improvement of stack-based piezoelectric generators. Renew. Energy *172*, 551–563. https://doi.org/10.1016/j.renene.2021.03.064.

14. Li, Z., Peng, X., Hu, G., Zhang, D., Xu, Z., Peng, Y., and Xie, S. (2022). Towards real-time self-powered sensing with ample redundant charges by a piezostack-based frequency-converted generator from human motions. Energy Convers. Manag. *258*, 115466. https://doi.org/10.1016/j.enconman.2022.115466.

15. Pan, M., Yuan, C., Liang, X., Zou, J., Zhang, Y., and Bowen, C. (2020). Triboelectric and piezoelectric nanogenerators for future soft robots and machines. iScience *23*, 101682. https://doi.org/10.1016/j.isci.2020.101682.

16. Xin, C., Li, Z., Zhang, Q., Peng, Y., Guo, H., and Xie, S. (2022). Investigating the output performance of triboelectric nanogenerators with single/double-sided interlayer. Nano Energy *100*, 107448. https://doi.org/10.1016/j.nanoen.2022.107448.

17. Shen, F., Zhang, D., Zhang, Q., Li, Z., Guo, H., Gong, Y., and Peng, Y. (2022). Influence of temperature difference on performance of solid-liquid triboelectric nanogenerators. Nano Energy *99*, 107431. https://doi.org/10.1016/j.nanoen.2022.107431.

18. Yin, P., Aw, K.C., Jiang, X., Xin, C., Guo, H., Tang, L., Peng, Y., and Li, Z. (2022). Fish gills inspired parallel-cell triboelectric nanogenerator. Nano Energy *95*, 106976. https://doi.org/10.1016/j.nanoen.2022.106976.

19. Zhang, Y., Wang, T., Luo, A., Hu, Y., Li, X., and Wang, F. (2018). Micro electrostatic energy harvester with both broad bandwidth and high normalized power density. Appl. Energy *212*, 362–371. https://doi.org/10.1016/j.apenergy.2017.12.053.

20. Honma, H., Tohyama, Y., Mitsuya, H., Hashiguchi, G., Fujita, H., and Toshiyoshi, H. (2021). Power enhancement of MEMS vibrational electrostatic energy harvester by stray capacitance reduction. J. Micromech. Microeng. *31*, 125008. https://doi.org/10.1088/1361-6439/ac2e46.

21. Yang, Z., Tang, L., Tao, K., and Aw, K. (2019). A broadband electret-based vibrational energy harvester using soft magneto-sensitive elastomer with asymmetrical frequency response profile. Smart Mater. Struct. *28*, 10LT02. https://doi.org/10.1088/1361-665x/ab3ae1.

22. Ueno, T. (2015). Performance of improved magnetostrictive vibrational power generator, simple and high power output for practical applications. J. Appl. Phys. *117*, 17A740. https://doi.org/10.1063/1.4917464.

23. Yu, J., Wen, Y., Yang, L., Zhao, Z., Guo, Y., and Guo, X. (2022). Monitoring on triboelectric nanogenerator and deep learning method. Nano Energy *92*, 106698. https://doi.org/10.1016/j.nanoen.2021.106698.

24. Garcia, C., and Trendafilova, I. (2019). Real-time diagnosis of small energy impacts using a triboelectric nanosensor. Sens. Actuator. A Phys. *291*, 196–203. https://doi.org/10.1016/j.sna.2019.03.044.

25. Zhao, T., Cao, S., Yang, S., Guo, R., Sang, S., and Zhang, H. (2019). A self-powered counter/timer based on a clock pointer-like frequency-tunable triboelectric nanogenerator for wind speed detecting. Nano Energy *65*, 104025. https://doi.org/10.1016/j.nanoen.2019.104025.

26. Zhang, H., Cheng, Q., Lu, X., Wang, W., Wang, Z.L., and Sun, C. (2021). Detection of driving actions on steering wheel using triboelectric nanogenerator via machine learning. Nano Energy *79*, 105455. https://doi.org/10.1016/j.nanoen.2020.105455.

27. Zhang, W., Wang, P., Sun, K., Wang, C., and Diao, D. (2019). Intelligently detecting and identifying liquids leakage combining triboelectric nanogenerator based self-powered sensor with machine learning. Nano Energy *56*, 277–285. https://doi.org/10.1016/j.nanoen.2018.11.058.

28. Liu, C., Wang, Y., Zhang, N., Yang, X., Wang, Z., Zhao, L., Yang, W., Dong, L., Che, L., Wang, G., and Zhou, X. (2020). A self-powered and high sensitivity acceleration sensor with V-Q-a model based on triboelectric nanogenerators (TENGs). Nano Energy *67*, 104228. https://doi.org/10.1016/j.nanoen.2019.104228.

29. Zhang, B., Wu, Z., Lin, Z., Guo, H., Chun, F., Yang, W., and Wang, Z.L. (2021). All-in-one 3D acceleration sensor based on coded liquid–metal triboelectric nanogenerator for vehicle restraint system. Mater. Today *43*, 37–44. https://doi.org/10.1016/j.mattod.2020.10.031.

30. Zhang, Z., He, J., Wen, T., Zhai, C., Han, J., Mu, J., Jia, W., Zhang, B., Zhang, W., Chou, X., and Xue, C. (2017). Magnetically levitated-triboelectric nanogenerator as a self-powered vibration monitoring sensor. Nano Energy *33*, 88–97. https://doi.org/10.1016/j.nanoen.2017.01.031.

31. Lu, X., Li, H., Zhang, X., Gao, B., and Cheng, T. (2022). Magnetic-assisted self-powered acceleration sensor for real-time monitoring vehicle operation and collision based on triboelectric nanogenerator. Nano Energy *96*, 107094. https://doi.org/10.1016/j.nanoen.2022.107094.

32. Phan, T.K., Wang, S., Wang, Y., Wang, H., Xiao, X., Pan, X., Xu, M., and Mi, J. (2020). A self-powered and low pressure loss gas flowmeter based on fluid-elastic flutter driven triboelectric nanogenerator. Sensors *20*, 729. https://doi.org/10.3390/s20030729.

33. Wang, Z., Yu, Y., Wang, Y., Lu, X., Cheng, T., Bao, G., and Wang, Z.L. (2020). Magnetic flap-type difunctional sensor for detecting pneumatic flow and liquid level based on triboelectric nanogenerator. ACS Nano *14*, 5981–5987. https://doi.org/10.1021/acsnano.0c01436.

34. Yao, H., Wang, Z., Wu, Y., Zhang, Y., Miao, K., Cui, M., Ao, T., Zhang, J., Ban, D., and Zheng,

H. (2022). Intelligent sound monitoring and identification system combining triboelectric nanogenerator-based self-powered sensor with deep learning technique. Adv. Funct. Mater. *32*, 2112155. https://doi.org/10.1002/adfm.202112155.

35. Ji, X., Zhao, T., Zhao, X., Lu, X., and Li, T. (2020). Triboelectric nanogenerator based smart electronics via machine learning. Adv. Mater. Technol. *5*, 1900921. https://doi.org/10.1002/admt.201900921.

36. Zhang, X., Zhao, J., Fu, X., Lin, Y., Qi, Y., Zhou, H., and Zhang, C. (2022). Broadband vibration energy powered autonomous wireless frequency monitoring system based on triboelectric nanogenerators. Nano Energy *98*, 107209. https://doi.org/10.1016/j.nanoen.2022.107209.

37. Du, T., Zuo, X., Dong, F., Li, S., Mtui, A.E., Zou, Y., Zhang, P., Zhao, J., Zhang, Y., Sun, P., and Xu, M. (2021). A self-powered and highly accurate vibration sensor based on bouncing-ball triboelectric nanogenerator for intelligent ship machinery monitoring. Micromachines *12*, 218. https://doi.org/10.3390/mi12020218.

38. Han, Q., Jiang, Z., Xu, X., Ding, Z., and Chu, F. (2022). Self-powered fault diagnosis of rolling bearings based on triboelectric effect. Mech. Syst. Signal Process. *166*, 108382. https://doi.org/10.1016/j.ymssp.2021.108382.

39. Zhao, X., Wei, G., Li, X., Qin, Y., Xu, D., Tang, W., Yin, H., Wei, X., and Jia, L. (2017). Self-powered triboelectric nano vibration accelerometer based wireless sensor system for railway state health monitoring. Nano Energy *34*, 549–555. https://doi.org/10.1016/j.nanoen.2017.02.036.

40. Park, J., Kim, I., Yun, J., and Kim, D. (2021). Liquid-metal embedded sponge-typed triboelectric nanogenerator for omnidirectionally detectable self-powered motion sensor. Nano Energy *89*, 106442. https://doi.org/10.1016/j.nanoen.2021.106442.

41. Li, X.H., Han, C.B., Jiang, T., Zhang, C., and Wang, Z.L. (2016). A ball-bearing structured triboelectric nanogenerator for nondestructive damage and rotating speed measurement. Nanotechnology *27*, 085401. https://doi.org/10.1088/0957-4484/27/8/085401.

42. Guo, R., Zhuo, K., Cui, X., Zhang, W., Sang, S., and Zhang, H. (2020). A triboelectric nanogenerator consisting of polytetrafluoroethylene (PTFE) pellet for self-powered detection of mechanical faults and inclination in dynamic mechanics. Energy Technol. *8*, 2000400. https://doi.org/10.1002/ente.202000400.

43. Chen, J., Zhang, C., Xuan, W., Yu, L., Dong, S., Xie, Y., Yin, W., and Luo, J. (2019). Triboelectric nanogenerator-based self-powered resonant sensor for non-destructive defect detection. Sensors *19*, 3262. https://doi.org/10.3390/s19153262.

44. Zeng, Q., Wu, Y., Tang, Q., Liu, W., Wu, J., Zhang, Y., Yin, G., Yang, H., Yuan, S., Tan, D., et al. (2020). A high-efficient breeze energy harvester utilizing a full-packaged triboelectric nanogenerator based on flow-induced vibration. Nano Energy *70*, 104524. https://doi.org/10.1016/j.nanoen.2020.104524.

45. Ren, Z., Wu, L., Zhang, J., Wang, Y., Wang, Y., Li, Q., Wang, F., Liang, X., and Yang, R. (2022). Trapezoidal cantilever-structure triboelectric nanogenerator integrated with a power management module for low-frequency vibration energy harvesting. ACS Appl. Mater. Interfaces *14*, 5497–5505. https://doi.org/10.1021/acsami.1c23309.

46. Zhao, C., Yang, Y., Upadrashta, D., and Zhao, L. (2021). Design, modeling and experimental validation of a low-frequency cantilever triboelectric energy harvester. Energy *214*, 118885. https://doi.org/10.1016/j.energy.2020.118885.

47. Zhao, S., Wu, N., and Wang, Q. (2016). Crack identification through scan-tuning of vibration characteristics using piezoelectric materials. Smart Mater. Struct. *26*, 025005. https://doi.org/10.1088/1361-665x/aa520a.

48. Deng, R., Lin, Y., Li, M., Gu, F., and Ball, A. (2022). Vision-based vibration mode shape extraction for identifying cracks in a cantilever beam. J. Phys, Conf. Ser. *2184*, 012037. https://doi.org/10.1088/1742-6596/2184/1/012037.

49. Samourgkanidis, G., and Kouzoudis, D. (2019). A pattern matching identification method of cracks on cantilever beams through their bending modes measured by magnetoelastic sensors. Theor. Appl. Fract. Mech. *103*, 102266. https://doi.org/10.1016/j.tafmec.2019.102266.

50. Suzuki, S., and Kondoh, J. (2021). Cantilever damage evaluation using impedance-loaded SAW sensor with continuous wavelet analysis and machine learning. Jpn. J. Appl. Phys. *60*, SDDC09. https://doi.org/10.35848/1347-4065/abf2d0.

51. Gupta, S.K., and Das, S. (2021). Damage detection in a cantilever beam using noisy mode shapes with an application of artificial neural network-based improved mode shape curvature technique. Asian J. Civ. Eng. *22*, 1671–1693. https://doi.org/10.1007/s42107-021-00404-w.

52. Zhao, S., Li, S., Guo, W., Zhang, C., and Cong, B. (2020). Quantitative diagnosis method of beam defects based on laser Doppler non-contact random vibration measurement. Measurement *152*, 107271. https://doi.org/10.1016/j.measurement.2019.107271.

53. Han, Q., Jiang, Z., Kong, Y., and Chu, F. (2022). Prebent membrane-based disk-type triboelectric nanogenerator applied to fault diagnosis in rotating machinery. IEEE ASME Trans. Mechatron. 1-11. 1, 11. https://doi.org/10.1109/TMECH.2022.3164022.

54. Chauhan, S., Singh, M., and Kumar Aggarwal, A. (2021). Bearing defect identification via evolutionary algorithm with adaptive wavelet mutation strategy. Measurement *179*, 109445. https://doi.org/10.1016/j.measurement.2021.109445.

55. Zhu, J., Wen, C., and Liu, J. (2022). Defect identification of wind turbine blade based on multi-feature fusion residual network and transfer learning. Energy Sci. Eng. *10*, 219–229. https://doi.org/10.1002/ese3.1024.

56. Han, T., Ma, R., and Zheng, J. (2021). Combination bidirectional long short-term memory and capsule network for rotating machinery fault diagnosis. Measurement *176*, 109208. https://doi.org/10.1016/j.measurement.2021.109208.

57. Shi, J., Peng, D., Peng, Z., Zhang, Z., Goebel, K., and Wu, D. (2022). Planetary gearbox fault diagnosis using bidirectional-convolutional LSTM networks. Mech. Syst. Signal Process. *162*, 107996. https://doi.org/10.1016/j.ymssp.2021.107996.

58. Yan, X., Guan, T., Fan, K., and Sun, Q. (2021). Novel double layer BiLSTM minor soft fault detection for sensors in air-conditioning system with KPCA reducing dimensions. J. Build. Eng. *44*, 102950. https://doi.org/10.1016/j.jobe.2021.102950.

59. Gandhi, C., Xiang, J., Kumar, A., Vashishtha, G., Kant, R., and Kant, R. (2022). Maximal overlap discrete wavelet packet transforms-based bipolar neutrosophic cross entropy measure for identification of rotor defects. Measurement *200*, 111577. https://doi.org/10.1016/j.measurement.2022.111577.

60. Tang, S., Zhu, Y., and Yuan, S. (2022). Intelligent fault identification of hydraulic pump using deep adaptive normalized CNN and synchrosqueezed wavelet transform. Reliab. Eng. Syst. Saf. *224*, 108560. https://doi.org/10.1016/j.ress.2022.108560.

61. Sun, Y., Cao, Y., and Li, P. (2022). Contactless Fault diagnosis for railway point machines based on multi-scale fractional wavelet packet energy entropy and synchronous optimization strategy. IEEE Trans. Veh. Technol. *71*, 5906–5914. https://doi.org/10.1109/TVT.2022.3158436.

STAR★METHODS

KEY RESOURCES TABLE

REAGENT or RESOURCE	SOURCE	IDENTIFIER
Chemicals, peptides, and recombinant proteins		
PI	Guangzhou (China) Beilong Electronics Co., Ltd	N/A
Sponge	Pinrao environmental protection material store (Taobao, China)	N/A
PTFE	3j flagship store (Taobao, China)	N/A
Graphite paper	Guangsheng Jiajin Metal New Material Store (Taobao, China)	N/A

RESOURCE AVAILABILITY

Lead contact

Further information and requests for resources and reagents should be directed to and will be fulfilled by the lead contact, Shaorong Xie (srxie@shu.edu.cn).

Materials availability

This study did not generate new materials. Materials used in the study are commercially available.

Data and code availability

All data reported in this paper will be shared by the lead contact upon reasonable request.

No new code was generated during the course of this study.

Any additional information required to reanalyze the data reported in this paper is available from the lead contact upon reasonable request.

EXPERIMENTAL MODEL AND SUBJECT DETAILS

This study does not use experimental methods typical in the life sciences.

METHOD DETAILS

Fabrication of CSF-TENG

All experimental materials such as polyimide (PI), sponge, polytetrafluoroethylene (PTFE), graphite paper (Gp), and nickel cloth were purchased from a local market (as shown in key resources table) and used without further treatment. The device attached to the positive triboelectric layer is made of aluminum material, so a 0.15 mm thick PI layer was used as a substrate to prevent the output performance of TENGs from being affected. Then, PTFE, Gp, and nickel cloth act as negative triboelectric layers, positive triboelectric layers, and electrodes, respectively, and their thicknesses are 0.05 mm, 0.05 mm, and 0.1 mm. The negative triboelectric layer was attached to an acrylic plate with a diameter of 40 mm, which was connected to cantilevers by screws. Compared to the negative triboelectric layer, the size of the positive triboelectric layer is larger, namely, 80 × 100 mm. Besides, to avoid the influence of wires on the contact area of triboelectric layers, the size of electrodes of negative triboelectric layers was set to 85 × 49.8 mm.

Electrical output signal measurement

The open-circuit voltages and short-circuit currents were measured by an oscilloscope (Tektronix MDO3024) and an electrometer (Keithley 6514), respectively.

QUANTIFICATION AND STATISTICAL ANALYSIS

The data were measured by an oscilloscope (Tektronix MDO3024) and an electrometer (Keithley 6514). Figures were produced by Origin from the raw data.

ADDITIONAL RESOURCES

This study has not generated or contributed to a new website/forum.